

## Role of rare earth sites and vacancies in the anomalous compression of modulated scheelite tungstates $RE_2(WO_4)_3$

Nanci Prado Sabalisk,<sup>1</sup> Gerardo Gil-de-Cos,<sup>1</sup> Cristina González-Silgo<sup>1,2,\*</sup>, Candelaria Guzmán-Afonso<sup>1</sup>, Víctor Lavín<sup>1</sup>, Javier López-Solano<sup>3</sup>, Isabel Teresa Martín-Mateos,<sup>4</sup> Lourdes Mestres<sup>5</sup>, Andrés Mujica<sup>1,2</sup>, David Santamaría-Pérez<sup>6</sup>, Manuel Eulalio Torres<sup>1,2</sup> and Xavier Vendrell<sup>7</sup>

<sup>1</sup>Departamento de Física, Universidad de La Laguna, San Cristóbal de La Laguna 38204, Spain

<sup>2</sup>Instituto de Materiales y Nanotecnología IMN, Universidad de La Laguna, San Cristóbal de La Laguna 38204, Spain

<sup>3</sup>Izaña Atmospheric Research Center, Agencia Estatal de Meteorología AEMET, Santa Cruz de Tenerife 38001, Spain

<sup>4</sup>Departamento de Ingeniería Industrial, Universidad de La Laguna, San Cristóbal de La Laguna 38204, Spain

<sup>5</sup>Departament de Química Orgànica e Inorgànica, Universitat de Barcelona, Barcelona 08028, Spain

<sup>6</sup>Departamento de Física Aplicada-ICMUV, Universitat de Valencia, Valencia 46980, Spain

<sup>7</sup>Institute of Energy Technologies, Universitat Politècnica de Catalunya, EEBE, Barcelona 08019, Spain

 (Received 8 July 2021; revised 11 October 2021; accepted 28 October 2021; published 3 December 2021)

X-ray powder diffraction experiments at high pressures combining conventional sources and synchrotron radiation, together with theoretical simulations have allowed us to study the anomalous compression of the entire  $\alpha$ - $RE_2(WO_4)_3$  ( $RE = \text{La-Ho}$ ) family with modulated scheelite structure ( $\alpha$  phase). The investigated class of materials is of great interest due to their peculiar structural behavior with temperature and pressure, which is highly sought after for specialized high-tech applications. Experimental data were analyzed using full-profile refinements and were complemented with computational methods based on density functional theory (DFT) total energy calculations for a subset of the samples investigated. An unusual change in the compression curves of the lattice parameters  $a$ ,  $c$ , and  $\beta$  was observed in both the experiments and theoretical simulations. In particular, in all the studied compounds the lattice parameter  $a$  decreased with pressure to a minimum value and then increased upon further compression. Pressure evolution of the experimental x-ray diffraction (XRD) patterns and cell parameters is correlated with the ionic radius of the rare earth element: (1) the lighter La-Nd tungstates underwent two phase transitions, and both transition pressures decreased as the rare earth's ionic radius increased. The XRD patterns of the first high pressure phase could be indexed with propagation vectors parallel to the  $a$  axis (tripling the unit cell). At higher pressures, the lattice parameters for the second phase (referred to as the *preamorphous* phase) showed little variation with pressure. (2) The heavier tungstates, from Sm to Dy, undergo a transition to the *preamorphous* phase without any intermediate phase. The reversibility of both phase transitions was investigated. DFT calculations support this unusual response of the crystal structures under pressure and shed light on the structural mechanism of negative linear compressibility (NLC) and the resulting softening. The pressure dependence of the structural modifications is related to tilting, along with small elongation and alignment, of the  $WO_4^{2-}$  tetrahedrons. These changes correlate with those in the alternating  $RE \dots RE \dots RE$  chains and blocks of cationic vacancies arranged along the  $a$  axis. Possible stacking defects, which emerge between them, helped to explain this anomalous compression and the pressure induced amorphization. Such mechanisms were compared with other ferroelastic families of molybdates, niobates, vanadates, and other compounds with similar structural motifs classified as having “hinge frames.”

DOI: [10.1103/PhysRevMaterials.5.123601](https://doi.org/10.1103/PhysRevMaterials.5.123601)

### I. INTRODUCTION

Pressure is a probe that triggers (and at the same time sheds light on) lattice instabilities, phase transitions, and even amorphization mechanisms, and it is thus an essential tool for producing new phases and emerging materials with tailored properties. Pressure affects directly the interatomic distances whereas temperature also induces changes in phonon-phonon

anharmonic interactions, and thus the competition between long- and short-range forces may be better understood by means of pressure alone [1]. Moreover, owing to its generally progressive nature, monitoring the pressure evolution of phase transitions and amorphization processes may be easier than studying their thermal dependence [2].

Rare earth, Y and Sc molybdates, and tungstates [ $RE_2(XO_4)_3$ , with  $X = \text{Mo}$  and  $\text{W}$ ] comprise a class of inorganic compounds that exhibit interesting physical properties, such as luminescence, ferroic, ionic, and electronic conductivity, and negative thermal expansion (NTE). All

\*csilgo@ull.edu.es

these properties have direct technological applications in their respective fields [3–6]. These materials exhibit a rich polymorphism in a range of temperatures and high pressures, making them good prototypes to probe new concepts about the physics of the structural phase transitions and counterintuitive structural properties like negative thermal expansion (NTE), negative linear compressibility (NLC) [7], and pressure-induced softening [8,9].

At ambient conditions, three polytypes without obvious symmetry relation among them are found. All the heavier tungstates and molybdates (with Y, Sc, and *RE* from Ho to Lu) belong to the  $\gamma$ - $\text{Sc}_2(\text{WO}_4)_3$ -type phase [10]. Lighter tungstates (from La to Ho) feature the  $\alpha$  phase described in  $\text{Eu}_2(\text{WO}_4)_3$ , which is a modulated scheelite-type structure [11]. Lighter molybdates from La to Nd feature the  $\text{La}_2(\text{MoO}_4)_3$ -type phase with another modulated scheelite-type structure [12]. For molybdates, if the rare earths have intermediate ionic radii (from Nd to Ho), two structural phases are found: the ferroelectric  $\beta'$ - $\text{Gd}_2(\text{MoO}_4)_3$  type [13] and the modulated scheelite  $\alpha$  phase which is also found in rare earth tungstates.

Special mention is deserved for the scheelite related compounds, which comprise, among others, the scheelites proper, as well as the wolframite and fergusonite types, and the modulated scheelites, which belong to a broad spectrum of compositions and polymorphs [14]. Their flexible cluster constituents, anionic  $\text{XO}_4$  tetrahedra and  $\text{AO}_8$  polyhedra, can be deformed within a wide range of temperatures and pressures resulting in a distorted electronic structure, which affects both the optical and electrical transport properties. Thus, their evolution under pressure has attracted new interest in the last years [15,16]. However, much less work has been devoted to  $\text{RE}_2(\text{XO}_4)_3$  compounds with modulated scheelite structure. The modulated scheelite structure is a cation deficient structure with formula  $(A, A')_n[(X, X')\text{O}_4]_m$ . The possibility to create cationic vacancies in the crystal lattice, with various orderings, is a factor in controlling the structural and physical properties of the modulated scheelite structure [17].

On the other hand, the interest on the amorphization of *RE* molybdates and tungstates stems from the evidence of pressure induced amorphization (PIA) in  $\beta'$ - $\text{Gd}_2(\text{MoO}_4)_3$  [18] at about 5 GPa, and the occurrence of a phase transition taking place before the amorphization. Among trimolybdates, more studies have been conducted to investigate the compression of the  $\beta'$  phase than for the  $\alpha$  phase. To our knowledge the following molybdates with  $\alpha$  phase are the only ones studied up to now:  $\text{Nd}_2(\text{MoO}_4)_3$ ,  $\text{Tb}_2(\text{MoO}_4)_3$  [19,20], and  $\text{Eu}_2(\text{MoO}_4)_3$  [21,22]. The only tungstate studied under high pressure is  $\text{La}_2(\text{WO}_4)_3$ , which undergoes two distinguishable phase transitions at high pressure compatible with the results of first-principles calculations [23].

Furthermore, within the emerging field of the effect of pressure on framework materials, the search for new NLC materials has been a focal point. They must be anisotropic [24] and own the specific structural motifs responsible for this anomalous effect. Cairns and Goodwin [8] have classified these mechanisms into four groups: compounds with ferroelastic phase transitions, with correlated polyhedral tilts, helical systems, and with “wine rack,” “honeycomb,” or related topologies. Interestingly, a strong anisotropy of the

crystal expansion and compression can support both NTE and NTC [25]. In addition, good candidates for pressure induced softening are both the anomalous thermal expansion and the proximity to a pressure-induced phase transition [26].

We are interested in the identification of the structural motifs that are involved in the underlying mechanisms which are responsible for these anomalous effects and their correlation with the observed physical properties of the  $\text{RE}_2(\text{XO}_4)_3$  family. For instance, the negative thermal expansion of the *a* parameter has been related to the electric properties of the  $\alpha$  phases of  $\text{Nd}_2(\text{MoO}_4)_3$ ,  $\text{Sm}_2(\text{MoO}_4)_3$ , and  $\text{Eu}_2(\text{MoO}_4)_3$  [27–29]. In addition, the NLC of the *a* lattice parameter has been observed for the  $\alpha$  phases of  $\text{Tb}_2(\text{MoO}_4)_3$  [20],  $\text{Eu}_2(\text{MoO}_4)_3$  [22], and  $\text{La}_2(\text{WO}_4)_3$  [23]. Accordingly, the extension of the high pressure studies to the  $\text{RE}_2(\text{WO}_4)_3$  family seems to be of interest. Additionally, the particular role played by the stoichiometric vacancies, arranging modulated structures, must be investigated because this family of compounds establishes a bridge between perfect and defect materials whose properties can vary widely.

In this work, we present a comprehensive study of the complete family of compounds  $\text{RE}_2(\text{WO}_4)_3$ , with  $\alpha$  phase, measured by conventional and synchrotron radiation. The study of the whole family provides a better picture than presenting each compound separately. An exhaustive analysis of the diffraction profiles, during compression and decompression, was carried out. The same refinement protocol has been used to obtain the evolution of the averaged lattice parameters with pressure. First-principles calculations have helped us to understand the evolution of the crystalline structure and to discuss possible mechanisms that lead to negative compression. Finally, results obtained by Sabalisck *et al.* [23] will be revisited in order to compare with other rare earth tungstates with  $\alpha$  phase.

## II. METHODS

### A. *Ab initio* calculations

For a selected group of members in the family [viz.  $\text{La}_2(\text{WO}_4)_3$ ,  $\text{Nd}_2(\text{WO}_4)_3$ ,  $\text{Gd}_2(\text{WO}_4)_3$ , and  $\text{Dy}_2(\text{WO}_4)_3$ ], total energy calculations were performed using the *ab initio* density functional theory (DFT) framework, in a scheme of a basis of plane waves and projector-augmented wave potentials (PAWs), as implemented in the VASP code [30–33]. The generalized gradient approximation was used for the exchange and correlation energy [34,35].

The  $5p^6$ ,  $5d^4$ , and  $6s^2$  electrons of W; and the  $2s^2$  and  $2p^4$  electrons of O were allowed to relax in the calculations for all the materials considered, with their remaining electrons being kept frozen in the core. For the rare earth elements in these materials the level of treatment of the *f* electrons corresponds to that in the library of recommended pseudopotentials of the VASP package. After testing, we have found it sufficient for the purpose of the present total energy study to take into account the valence of the  $5s^2$ ,  $5p^6$ ,  $6d^1$ , and  $6s^2$  electrons for La; the  $5s^2$ ,  $5p^6$ ,  $4f^1$ , and  $6s^2$  for Nd; the  $5p^6$ ,  $5d^1$ , and  $6s^2$  for Gd; and the  $5p^6$ ,  $4f^1$ , and  $6s^2$  for Dy. The calculations were performed using the generalized gradient approximation (GGA) of the

exchange-correlation (XC) energy functional as originally defined by Perdew, Burke, and Ernzerhof (PBE) [34], and their revised PBEsol form [35].

In all cases, the cutoff in the kinetic energy of the plane waves entering in the calculations was 520 eV which, together with  $4 \times 4 \times 2$  integration grids in  $k$  space [36] for the  $\alpha$  phase, ensures a relative convergence of a few meV per formula unit. For each material and for each fixed volume a full geometrical optimization under hydrostatic conditions of both the cell shape and the atomic positions was performed. The relaxation was considered complete when the calculated forces on atoms were less than  $0.005 \text{ eV/\AA}$  and the calculated stress tensor was diagonal with the difference between diagonal components less than 0.1 GPa. All calculations were done at zero temperature and the small effect of the zero-point energy was not taken into account.

### B. Synthesis

Ten  $RE = \text{La-Ho}$  tungstates (excluding Pm, a radioactive element) were prepared by the conventional solid-state reaction route from the corresponding raw, high purity oxides  $RE_2O_3$  (Alfa Aesar, 99.99%) and  $H_2WO_4$  (Aldrich, 99%). Rare earth oxides were calcined prior to use at 1173 K for 8 h. The reagents were weighed, according to the desired stoichiometric composition, mixed, and homogenized (thoroughly ground in an agate mortar) using acetone as the grinding media. The obtained powders were pressed to produce disk-shaped samples by applying 100 MPa of uniaxial pressure. The pellets were heated twice for 7 h at 1273 K under air atmosphere and were further heat treated at 1273 K for 15 h after regrinding. A moderate cooling rate of 100 K/h was used to reach 323 K and it remained at this temperature in the furnace for 24 h. After this thermal treatment the samples were taken out of the furnace for further analysis.

### C. Powder diffraction

In order to identify the  $\alpha$  phase and check the purity of the sample, x-ray patterns were measured at room conditions, by continuous scanning with a step of  $1^\circ/\text{min}$  in the angular range  $10^\circ < 2\theta < 80^\circ$ , using a PANalytical XPert PRO diffractometer (Bragg-Brentano mode). A primary monochromator of Ge(111) and an X'Celerator detector for  $K\alpha_1$  copper radiation (generated at 40 kV and 30 mA) were used.

All the samples were experimentally characterized by x-ray powder diffraction under high pressure using both an in-house source as well as synchrotron radiation at the ALBA and DIAMOND synchrotron sources. The *in situ* pressures were measured using the ruby fluorescence technique and the pressures for the different experiments are given in Supplemental Material Tables S1a, S1b, and S1c [37].

Angle-dispersive x-ray diffraction measurements were carried out with an Xcalibur diffractometer for the  $RE_2(WO_4)_3$  ( $RE = \text{La-Nd}$ ) samples. X-ray diffraction patterns were obtained on a 135-mm Atlas charge-coupled device (CCD) detector placed 110 mm from the sample using  $K\alpha_1 : K\alpha_2$  molybdenum radiation. The x-ray beam was collimated to a diameter of  $300 \mu\text{m}$ . The observed intensities were integrated as a function of  $2\theta$  in order to give conventional

one-dimensional diffraction profiles. Exposure times were typically 1 h. The diamond cells used for these experiments allowed access to an angular range  $4\theta = 50^\circ$ . The CRYCALIS software (version 171.34.49, Oxford Diffraction Limited) was used for the collection and preliminary reduction of the data. High-pressure measurements on the four polycrystalline samples were performed in two modified Merrill-Bassett diamond anvil cells (DACs) up to a pressure of 18 GPa. A mixture of methanol/ethanol (4:1) was used as pressure-transmitting medium.

Two different angle-dispersive x-ray diffraction experiments (codes 2012010246 and 2012100359, hereafter ALBA1 and ALBA2, respectively) were carried out on  $RE_2(WO_4)_3$  ( $RE = \text{La, Nd, Sm, Gd, and Dy}$ ) samples at the MSPD04 at ALBA beamline (Barcelona, Spain) using monochromatic radiation with  $\lambda = 0.4246(1) \text{ \AA}$  and  $\lambda = 0.4183(3) \text{ \AA}$ , respectively. The data were collected using a Rayonix SX165 CCD detector, placed 300–400 mm from the sample with 20 s of exposition time and  $4^\circ$  in  $\varphi$  rotation angle. Pressures were generated with different diamond-anvil cells. We used (a) two mini-Bragg cells from Easylab Co. with an aperture angle of  $85^\circ$  and equipped with steel gaskets, and (b) a MiniDAC made at the University of Paderborn, with an angle aperture of  $40^\circ$  and equipped with Inconel X-750 gaskets. In these experiments a mixture of methanol-ethanol-water (16:3:1) was used as pressure-transmitting medium.

Furthermore, powder diffraction experiments at high pressure were carried out in DIAMOND. The polycrystalline  $RE_2(WO_4)_3$  ( $RE = \text{Eu, Tb, and Ho}$ ) powder was measured with a synchrotron radiation source [ $\lambda = 0.4130(2) \text{ \AA}$ , after the latest refinement] equipped with a MAR345 image plate detector at the Beamline I15 of the Diamond Light Source (experiment code EE8617). The samples were loaded into the diamond-anvil pressure cell (MiniDAC of the University of Paderborn), with an aperture angle of  $40^\circ$ , equipped with Inconel gaskets and using a mix of methanol-ethanol-water 16:3:1 as pressure-transmitting medium.

### D. Data analysis

The collected intensities were integrated as a function of the  $2\theta$  angle using the FIT2D software [38]. The x-ray diffraction (XRD) patterns collected at room conditions were refined by iterating full pattern profile fitting with the Le Bail (2005) [39] method using the FULLPROF software [40] and starting from the structural parameters of the  $\alpha\text{-Eu}_2(WO_4)_3$ . The background was modeled by a Chebychev polynomial with six refinable coefficients.

Compared to those collected at room conditions, powder XRD at high pressure suffers from several drawbacks and simultaneous parametric refinement have several advantages [41]. Accordingly, each set of one-dimensional (1D) patterns (for one rare earth tungstate) was refined using this non-conventional refinement. Starting cell parameters were the theoretical ones at all pressures. These cell parameters were refined simultaneously and constrainedly for each compound, taking into account multiple phases at different pressures with their corresponding patterns. In the last refinement, all parameters were unconstrained. The background was modeled by a linear interpolation between points. Because the angular

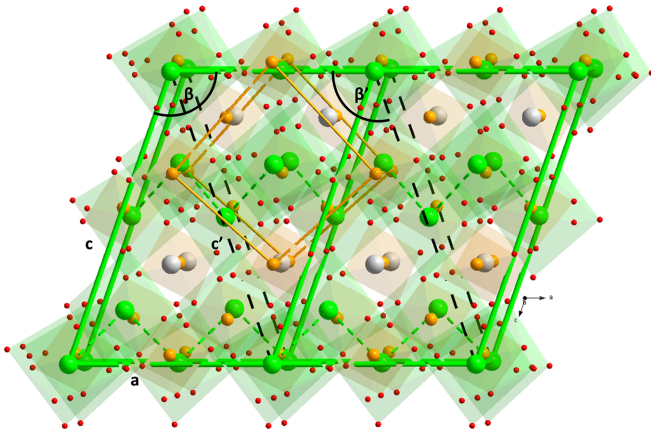


FIG. 1. A  $b$  axis view of the  $\alpha$ - $\text{Eu}_2(\text{WO}_4)_3$  structure. Orange and green lines show the parent scheelite and the  $\alpha$ -phase unit cell, respectively. Tungsten and europium atoms and their corresponding tetrahedra and polyhedra are colored in orange and green, respectively. Vacancies are colored in gray. Black dashed lines draw the unconventional  $c'$  parameter.

aperture is too small, the background is truncated, losing the asymptotic behavior, and it is very difficult to fit it with a polynomial.

The profile parameters were refined starting from the instrumental resolution function (Thomson-Cox-Hastings pseudo-Voigt with axial divergence asymmetry) where the parameters  $U$  and  $X$ , which relate to the microstrains and grain or domain size, respectively, were refined.

In order to improve the refinement at the intermediate and the *preamorphous* phase, possible satellite peaks were tentatively indexed using propagation vectors, as we will explain in Sec. III.

All graphics were plotted with the software ORIGINLAB [42] and all the crystal structures were drawn with the software DIAMOND - CRYSTAL AND MOLECULAR STRUCTURE VISUALIZATION [43]. The fitting of the pressure and volume to an equation of state was further checked with the software EOSFIT7-GUI [44].

### III. DISCUSSION

#### A. Modulated scheelite structure of the $\alpha$ phase

All of the different  $\text{RE}_2(\text{WO}_4)_3$  materials ( $\text{RE} = \text{La}, \text{Ce}, \text{Pr}, \text{Nd}, \text{Sm}, \text{Gd}, \text{Tb}, \text{Dy}, \text{and Ho}$ ) crystallize in the  $\alpha$  phase at room conditions. A few impurity peaks in  $\text{Ce}_2(\text{WO}_4)_3$  and  $\text{Dy}_2(\text{WO}_4)_3$  were identified as starting oxides ( $\text{WO}_3$  or  $\text{RE}_2\text{O}_3$ ), but they were unrecognizable in the experiments under pressure. In the case of  $\text{Ho}_2(\text{WO}_4)_3$ , some small peaks, at low angles, which belonged to the  $\gamma$ - $\text{Sc}_2(\text{WO}_4)_3$  phase [6], were identified but this phase was not refined (it is hydrated at room conditions). Impurities of  $\text{RE}_2\text{W}_2\text{O}_9$  were detected in some cases for  $\text{Sm}_2(\text{WO}_4)_3$ ,  $\text{Eu}_2(\text{WO}_4)_3$ , and  $\text{Gd}_2(\text{WO}_4)_3$ . In Fig. S1 and Fig. S2 in the Supplemental Material [37], we show all the routine diffractograms and their adjustments.

In this family of compounds, the  $\alpha$  phase [ $\text{Eu}_2(\text{WO}_4)_3$ -structure type [11]] has space group  $C2/c$  with four formula units per crystallographic unit cell. Its asymmetric unit con-

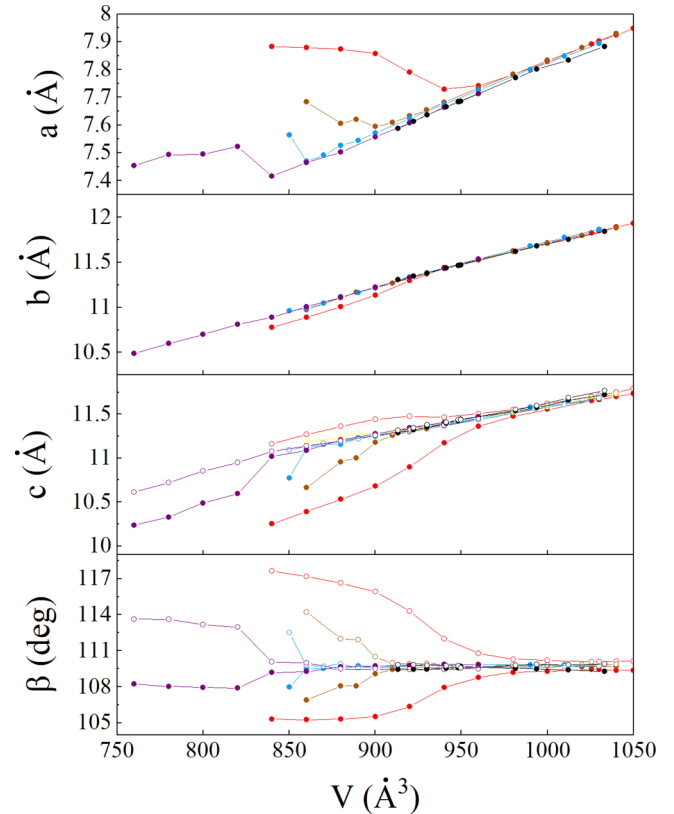


FIG. 2. Volume dependence of the experimental lattice parameters of  $\text{RE}_2(\text{WO}_4)_3$  compounds ( $\text{RE} = \text{La}, \text{Ce}, \text{Pr}, \text{Nd}, \text{Sm}, \text{Eu}, \text{Gd}, \text{Dy}, \text{Tb}, \text{and Ho}$ ) at room temperature (in black) and the theoretical ones for  $\text{RE} = \text{La}$  (red),  $\text{Nd}$  (yellow),  $\text{Gd}$  (blue), and  $\text{Dy}$  (violet). Open symbols indicate the  $c'$  and  $\beta'$  parameters.

tains nine atoms with all nonequivalent positions of the general type  $8f$ , except for the  $\text{W}$  atom which occupies  $4e$  positions (with  $C2$  site symmetry). There are two  $\text{Eu}$  atoms and one stoichiometric vacancy for every three  $\text{W}$  atoms. This structure type can be described as a cation-deficient structure with formula  $(A, A')_n[(\text{XO}_4)_m]$  where  $n = 2$  and  $m = 3$  in the monoclinic superspace group  $I_2/b(\alpha\beta 0)00$ , with a modulation vector  $\mathbf{k} = 2a^*/3 + 2b^*/3$ , with  $a^*$  and  $b^*$  the reciprocal lattice parameters [45]. In Fig. 1 we show a view of the crystal structure along the  $b$  axis: the scheelite parent cell is marked by orange lines and the cell of the  $\alpha$  phase is marked in green, with the vacancies in the tungsten sites aligned along the  $a$  axis. Shorter contacts between  $\text{Eu}$  atoms are displayed. This symmetry makes it possible to define the unit cell in two ways, similarly to the ferroelastic compounds, by choosing two different  $c$  lattice parameters ( $c$  or  $c'$ ) related by  $c' = c - a$  (see the dashed black lines in Fig. 1). Because both cells describe the same crystallographic lattice, we have chosen the set of lattice parameters in which the monoclinic angle  $\beta$  and the lattice parameter  $c$  decrease under applied pressure as well as when the ionic radius decreases. This rule is not always observed in the published literature, for example, the  $\beta$  angle of europium molybdate [22] behaves in the opposite way as in  $\text{La}_2(\text{WO}_4)_3$  [23] or  $\text{Tb}_2(\text{MoO}_4)_3$  [20]. Similarly, the thermal dependence of  $\beta$  in the  $\text{Sm}$  and  $\text{Eu}$  molybdates [27,28] feature

TABLE I. Lattice parameters at approximately 0 GPa from experimental (routine and under pressure) and theoretical results.

	$a$ (Å)	$b$ (Å)	$c$ (Å)	$\beta$ (deg)	$V$ (Å <sup>3</sup> )
<b>La<sub>2</sub>(WO<sub>4</sub>)<sub>3</sub></b>					
Expt. routine 0 GPa	7.8829(2)	11.8443(3)	11.7238(3)	110.103(1)	1027.93(4)
Exp 0.0 GPa	7.871(3) <sup>a</sup>	11.828(5) <sup>a</sup>	11.643(6) <sup>a</sup>	110.103(1) <sup>a</sup>	1023.2(4) <sup>a</sup>
Theor. 0.0GPa	7.910 <sup>a</sup>	11.789 <sup>a</sup>	11.670 <sup>a</sup>	109.468 <sup>a</sup>	1026 <sup>a</sup>
<b>Nd<sub>2</sub>(WO<sub>4</sub>)<sub>3</sub></b>					
Expt. routine 0 GPa	7.7698(2)	11.6214(3)	11.5366(3)	109.547(2)	981.67(4)
Expt. 0.0 GPa	7.756(7)	11.60(2)	11.51(2)	109.4(2)	977(2)
Theor. -0.54 GPa	7.930	11.882	11.721	109.672	980
Theor. 1.09 GPa	7.879	11.795	11.655	109.660	960
<b>Gd<sub>2</sub>(WO<sub>4</sub>)<sub>3</sub></b>					
Expt. routine 0 GPa	7.6653(2)	11.4341(3)	11.3941(4)	109.541(2)	941.13(5)
Expt. 1.5 GPa	7.614(2)	11.35(1)	11.345(1)	109.69(1)	923.6(2)
Theor -0.38 GPa	7.798	11.664	11.541	109.405	940
Theor. 1.40 GPa	7.726	11.518	11.436	109.152	920
<b>Dy<sub>2</sub>(WO<sub>4</sub>)<sub>3</sub></b>					
Expt. routine 0GPa	7.6135(2)	11.3474(3)	11.3208(3)	109.452(2)	922.21(4)
Expt. 0.16 GPa	7.563(1)	11.2751(2)	11.236(2)	109.22(2)	904.7(2)
Theor. -0.20 GPa	7.713	11.535	11.471	109.835	920
Theor. 1.6 GPa	7.663	11.438	11.403	109.866	900

<sup>a</sup>Values from Ref. [23].

the opposite behavior, so that when the volume increases, the monoclinic angle decreases.

The volume dependence of our experimental lattice parameters and the theoretical ones are shown in Fig. 2 and lattice parameters at room conditions are compared in Table I. All the  $a$ ,  $b$ , and  $c$  parameters decrease monotonically when the volume (ionic radii) increases from La to Ho and when the fixed volume (pressure) increases for each compound simulated: La<sub>2</sub>(WO<sub>4</sub>)<sub>3</sub>, Nd<sub>2</sub>(WO<sub>4</sub>)<sub>3</sub>, Gd<sub>2</sub>(WO<sub>4</sub>)<sub>3</sub>, and Dy<sub>2</sub>(WO<sub>4</sub>)<sub>3</sub>. Both  $\beta'$  and  $c'$  parameters are also depicted in Fig. 2 in order to show the anisotropic behavior expected when the samples are subjected to high pressure. To provide a fuller discussion of the compressibility of the unit-cell axes, we will show the directions of minimum and maximum compression in the  $ac$  plane.

### B. Pressure evolution of the Bragg peaks

In Fig. 3, XRD patterns and selected refinements for the La<sub>2</sub>(WO<sub>4</sub>)<sub>3</sub>, Nd<sub>2</sub>(WO<sub>4</sub>)<sub>3</sub>, Gd<sub>2</sub>(WO<sub>4</sub>)<sub>3</sub>, and Dy<sub>2</sub>(WO<sub>4</sub>)<sub>3</sub> compounds are shown. The corresponding figures for the remaining compounds are shown in the Supplemental Material (Figs. S3) [37]. Diffractograms collected under hygroscopic conditions could be fitted with average unit cells within the monoclinic space group  $C2/c$ , corresponding to the  $\alpha$  phase. The Le Bail refinements were of good quality (see Table S2 in the Supplemental Material [37]). Furthermore, Fig. 4 shows the theoretical  $d_{hkl}$  (filled circles) and experimental  $d_{hkl}$  (open circles) vs cell volume.

The results from the Xcalibur experiment for the four lighter compounds were very similar. A sudden splitting that starts at 3.8 GPa for La<sub>2</sub>(WO<sub>4</sub>)<sub>3</sub>, at 4.65 GPa for Ce<sub>2</sub>(WO<sub>4</sub>)<sub>3</sub>, at 5.38 GPa for Pr<sub>2</sub>(WO<sub>4</sub>)<sub>3</sub>, and at 6.57 GPa for Nd<sub>2</sub>(WO<sub>4</sub>)<sub>3</sub> indicates just a small crystallographic unit cell deformation, confirmed by the anisotropic behavior of the interplanar spac-

ing. By increasing the pressure, satellite reflections (with propagation vector  $\mathbf{k} = \mathbf{a}^*/3$ ) were used to refine weak peaks, which appeared between  $2\theta = 12^\circ$  and  $14^\circ$  up to 6.45 GPa for La<sub>2</sub>(WO<sub>4</sub>)<sub>3</sub>, 6.00 GPa for Ce<sub>2</sub>(WO<sub>4</sub>)<sub>3</sub>, 8.35 GPa for Pr<sub>2</sub>(WO<sub>4</sub>)<sub>3</sub>, and 9.7 GPa for Nd<sub>2</sub>(WO<sub>4</sub>)<sub>3</sub>, respectively. The appearance of these new weak peaks does not affect the evolution of the main reflections and their respective  $d_{hkl}$  distances. These changes can be considered as a first phase transition in which the cell parameter  $a$  is tripled and the symmetry is preserved in the same space group. Thus, the new phase belongs to a *klassengleich* maximal subgroup with index = 3. In the Supplemental Material (Figs. S4 and S5) [37], we have simulated a possible small distortion using the software AMPLIMODES [46] from the Bilbao Crystallographic Server [47]. All possible maximal supergroups with index = 2 were tested without success and there are no subgroups with double  $a$  axis compatible with this space group. This result is compatible with the coexistence of two or more  $\alpha$  phases with the same space group, in agreement with the *ab initio* finding of multiple structurally related structures with similar enthalpies [23]. These superstructures occur when the larger coordination polyhedron volume of the lanthanides with larger ionic radii leads to structural instability. In the case of  $RE_2(\text{MoO}_4)_3$  molybdates, compounds with  $RE = \text{La, Ce, Pr, and Nd}$  have triple cell volumes compared to compounds with  $RE = \text{Sm, Eu, Gd, Tb, Dy, and Ho}$  with  $\alpha$  phase [12]. In the double molybdate family  $KRE(\text{MoO}_4)_2$  ( $RE = \text{Eu, Gd, and Tb}$ ) the  $\alpha$  phase has a distorted scheelite structure while the  $\beta$  phase ( $RE = \text{Pr, Nd, and Sm}$ ) has an incommensurate superstructure [48].

In addition, the  $\alpha$  phase was recovered after being released from 7.44 GPa for La<sub>2</sub>(WO<sub>4</sub>)<sub>3</sub>, and this fact reinforces the hypothesis of a reversible second-order phase transition.

Up to the mentioned pressures, the diffractions peaks continue shifting towards higher angles as is expected for a

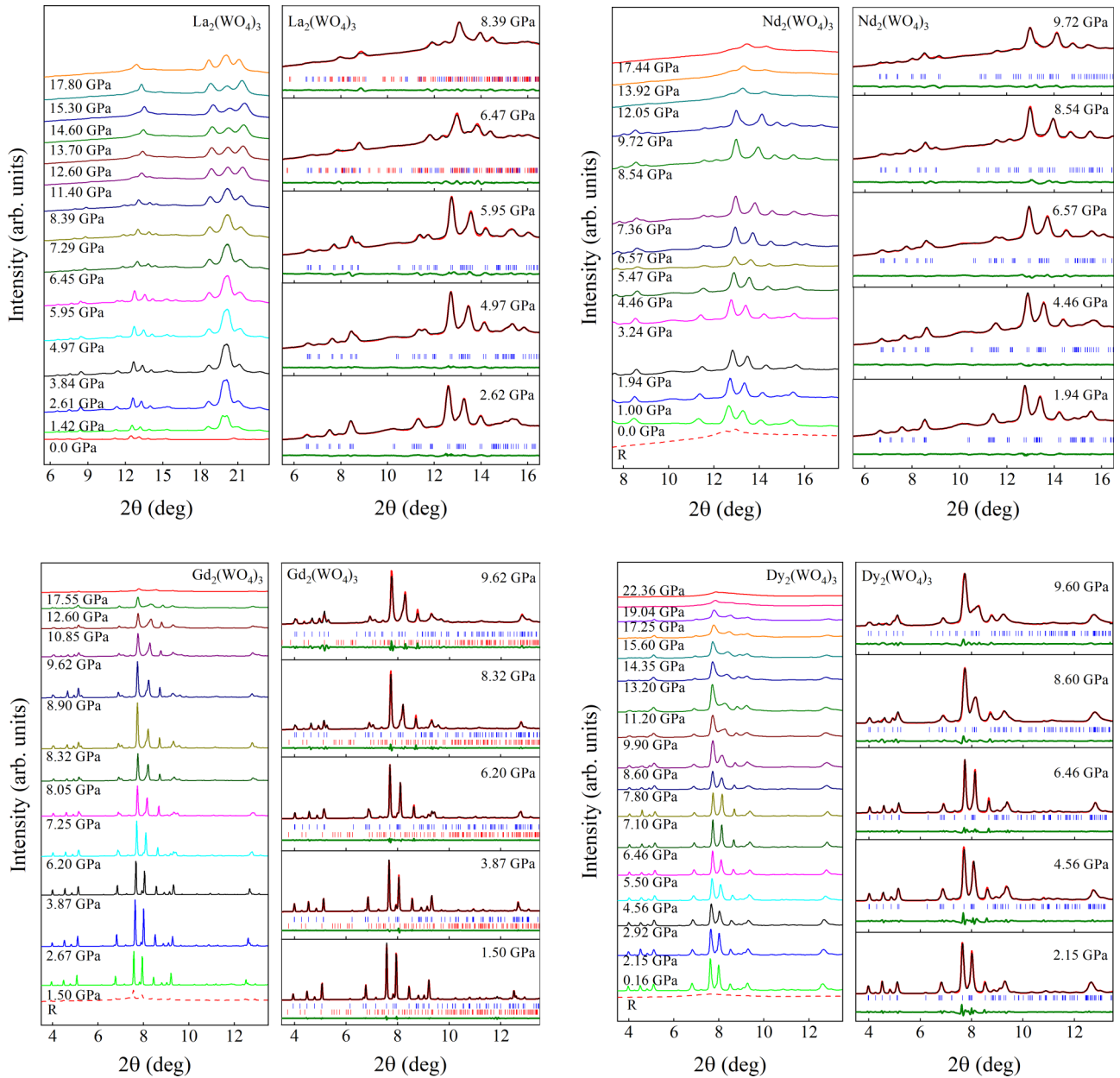


FIG. 3. Left: Diffraction patterns of selected  $RE_2(WO_4)_3$  compounds ( $RE = La, Nd, Gd,$  and  $Dy$ ) at different pressures measured in GPa, given as a label by the corresponding diffractogram. In the patterns refined at selected pressures (right), the experimental results (red lines) are shown together with the calculated patterns (black lines). The blue sticks indicate the positions of Bragg reflections for the  $\alpha$  phase. Satellite peaks are marked with red sticks. Patterns with the label R correspond to released pressures.

material with long range ordering upon compression until 11.4 GPa for  $La_2(WO_4)_3$ , 12.70 GPa for  $Ce_2(WO_4)_3$ , 14.90 GPa for  $Pr_2(WO_4)_3$ , and 13.90 for  $Nd_2(WO_4)_3$ . From these pressures, the observed changes in the line profile suggest nonetheless that a new phase transition has taken place. Similar patterns persist after a little broadening and without an important shift of the peaks. Henceforth, we will refer to this structure as the *preamorphous* phase. Up to the maximum pressure reached of around 18 GPa the action of deviatoric stresses associated with nonhydrostatic conditions may affect the quality of the diffraction patterns (deteriorating the signal to background ratio and producing line broadening [49]). Some authors increase the range of working pressures (up to

30 GPa) with methanol-ethanol-water as pressure transmission medium and they do not observe a substantial broadening of the diffraction peaks belonging to ruby crystals [50]. In our case, the broadening that we observed may also be associated with the compression of the *preamorphous* phase, which we will explain below. In addition, during the pressure release from 17.8, 17.7, 17.3, and 17.4 GPa for, respectively,  $La_2(WO_4)_3$ ,  $Ce_2(WO_4)_3$ ,  $Pr_2(WO_4)_3$ , and  $Nd_2(WO_4)_3$ , the *preamorphous* phase presented similar line shapes to those measured at 11.4, 12.70, 12.90, and 13.90 GPa, respectively, showing an irreversible degradation of the diffraction signal. The  $\alpha$  phase was not recovered, so we can consider an irreversible transition to this new phase

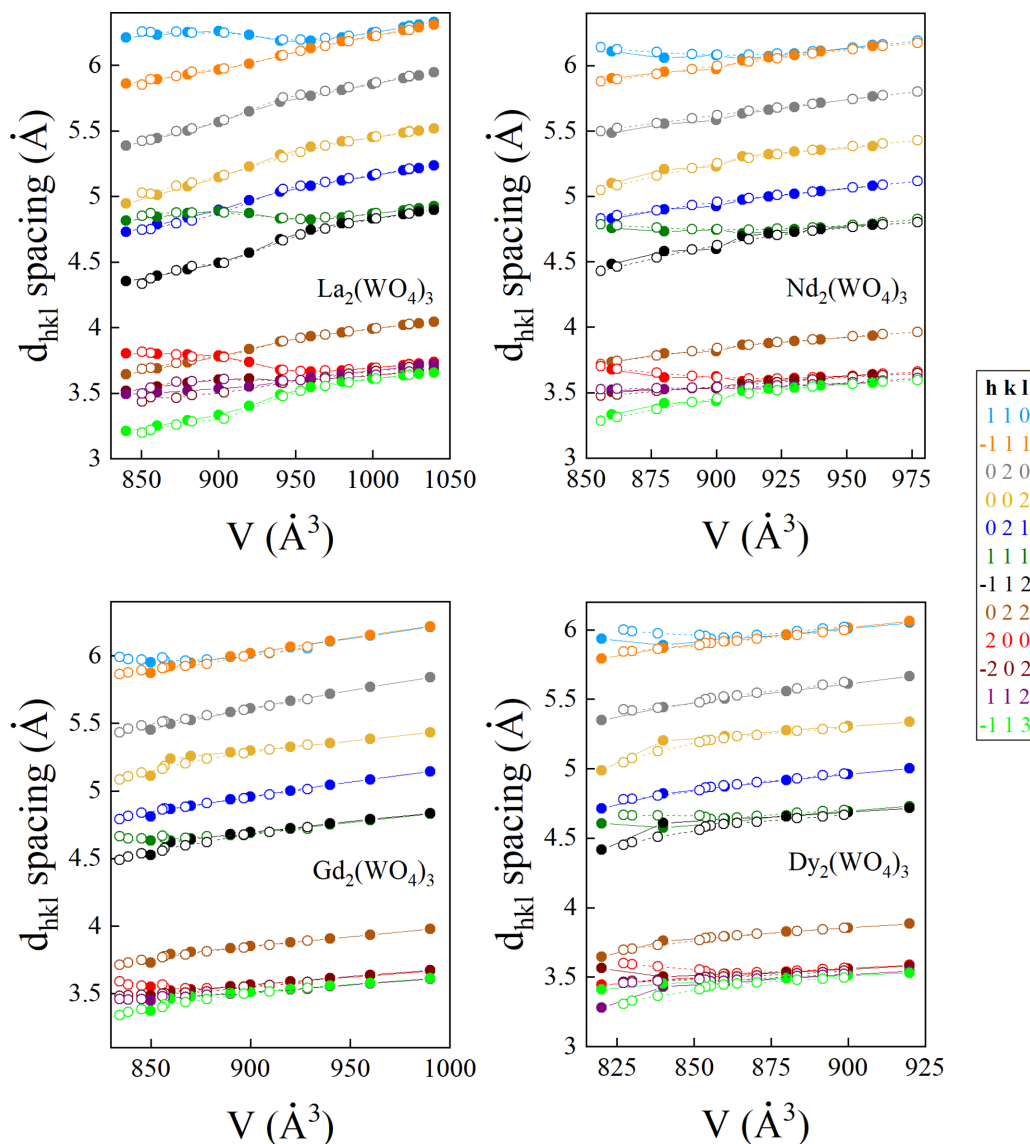


FIG. 4. Theoretical and experimental volume dependence of different  $d_{hkl}$  interplanar distances for  $RE_2(WO_4)_3$  cell ( $RE = La, Nd, Gd,$  and  $Dy$ ). In all cases the filled circles correspond to theoretical values whereas the empty circles are experimental results, and lines are just a guide for the eye.

(around the given pressures). When the pressure is completely released, the broad peaks of the *preamorphous* phase shift to lower angles, indicating some structural relaxation.

The experiments for  $La_2(WO_4)_3$  (ALBA1) from 0 to 10.2 GPa and  $Nd_2(WO_4)_3$  (ALBA2) from 0.75 to 15.9 GPa confirmed the anomalous compression of these compounds, in which two phase transitions take place: satellite peaks appear at the same pressures (at 6.2 and 8.1 GPa, respectively) and the *preamorphous* phase appears between 10.40 and 12.0 GPa for  $Nd_2(WO_4)_3$  GPa and between 9.7 and 11.4 GPa for  $La_2(WO_4)_3$ , then the  $\alpha$  phase was not completely recovered for the released sample, because the decompression started from the last pressure reached (in the *preamorphous* phase). The experiments on ALBA1 were not optimal, and the diffractograms were not refined, as explained above, but have been shown in the Supplemental Material (Fig. S3e) [37].

A less similar behavior can be described for the heavier  $RE_2(WO_4)_3$  ( $RE = Sm-Ho$ ). Figure 3 and Fig. S3, in the Supplemental Material [37], show the pressure evolution of the XRD patterns in these compounds where higher quality data than in previous experiments can be appreciated (they were measured using synchrotron radiation).

Regarding the compounds measured in the ALBA2 experiments, we do not observe any clear first phase transition, although the compression is more anisotropic at higher pressures than for lower ones. Some peaks were splitting at 7.14 GPa for  $Sm_2(WO_4)_3$ , at 7.1 GPa for  $Eu_2(WO_4)_3$ , at 7.25 GPa for  $Gd_2(WO_4)_3$ , and at 7.8 GPa for  $Dy_2(WO_4)_3$ . These peaks separate as the pressure increases. The evolution of the  $d_{hkl}$  of  $Gd_2(WO_4)_3$  and  $Dy_2(WO_4)_3$  can also be seen in Fig. 4. At 12.11 GPa for  $Sm_2(WO_4)_3$ , before 15.20 GPa for  $Eu_2(WO_4)_3$ , at 12.60 GPa for  $Gd_2(WO_4)_3$ , and at 13.20 GPa for  $Dy_2(WO_4)_3$ , the lattice parameters were not refined. The Bragg peaks have broadened, and an amorphous component

has arisen in the pattern. Above these pressures, in the cases in which higher pressures were measured (after 17 GPa for Gd and Dy), similar patterns persist without a clear shift towards low angles of the peaks. We consider again the formation of a *preamorphous* phase, like in the lighter tungstates; although the data were collected at nonhydrostatic conditions. When the pressure is released from these values, the initial phase is partially recovered.

For the experiments performed at the synchrotron DIAMOND, it was not possible to reach the *preamorphous* phase in the pressure range studied:  $\text{Eu}_2(\text{WO}_4)_3$  from 0.2 to 5.8 GPa;  $\text{Tb}_2(\text{WO}_4)_3$  from 0.3 to 8.5 GPa; and  $\text{Ho}_2(\text{WO}_4)_3$  from 0.4 to 8.4 GPa. Thus, the decompression process was found to be reversible for all three samples—all of them recover their initial phases, independently of the value of the pressure at the beginning of the unloading. Similarly, to other heavier tungstates, some peaks were splitting at 7.6 GPa for  $\text{Tb}_2(\text{WO}_4)_3$  and at 7.9 GPa for  $\text{Ho}_2(\text{WO}_4)_3$ . The results for Sm, Eu, Gd, Tb, and Ho tungstates are similar to previous XRD and the Raman spectroscopy studies for pressurized  $\text{Eu}_2(\text{MoO}_4)_3$  [21,22] and  $\text{Tb}_2(\text{MoO}_4)_3$  [19,20] molybdates. There is not a clear phase transition but these compounds display important anomalies between 7–8 and 12–13 GPa.

As a last result of this subsection, we reached the complete amorphization of  $\text{Dy}_2(\text{WO}_4)_3$  at 22.36 GPa (see Fig. 3). The process was completely irreversible. The sample was released down to 15 GPa maintaining the amorphous phase. In previous experiments, the  $\alpha$  phase was always partially obtained after the release, probably because a complete amorphization was never reached. Before that, satellite peaks were refined with a propagation vector  $\mathbf{k} = \mathbf{a}^*/3$  at 13.2 GPa, like for the other lighter tungstates but at higher pressure. The appearance of these new weak peaks does not affect the evolution of the main reflections, whose  $d_{hkl}$  distances agree with the theoretical ones (Fig. 4). This refinement was not possible for the samarium and gadolinium tungstates because impurities' peaks overlapped with possible satellite ones.

Irreversibility of the transition to the *preamorphous* phase could be related to the formation of stacking faults, as we discuss in Sabalisck *et al.* [23]. This process has been suggested in the case of the incommensurate structure of  $\text{Pr}_2(\text{MoO}_4)_3$ , where the coexistence of different rearrangements of the vacancies is possible [51]. A completely amorphous phase could be thus explained as an assemblage of a large number of structures with stacking faults generated through an irreversible mechanism [52]. This process is more feasible and probably more abrupt when vacancies have larger sizes (rare earths with longer ionic radius). The degree of recovering depends on the maximum pressure reached and therefore on the degree of the amorphization. For the tungstates of rare earths with smaller ionic radii, the phase transitions are not so clear as the stacking faults develop rather sluggishly. Moreover, the amorphization in molybdates is expected around 20–25 GPa [19,21], similar to  $\text{Dy}_2(\text{WO}_4)_3$ . A transition to a *preamorphous* phase has not been discussed in rare earth molybdates, although it seems feasible.

### C. Unit cell compression and phase diagram

As we see in Fig. 4, the theoretical and experimental  $d$  spacing are in very good agreement for the more anisotropic

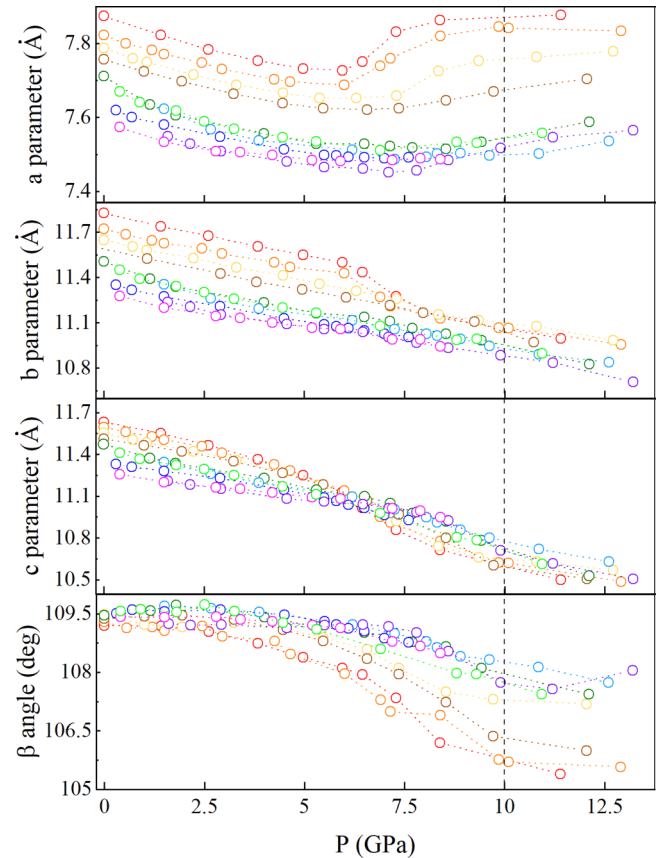


FIG. 5. Pressure dependence lattice parameters  $a$ ,  $b$ ,  $c$ , and  $\beta$  for  $\text{La}_2(\text{WO}_4)_3$  (red),  $\text{Ce}_2(\text{WO}_4)_3$  (orange),  $\text{Pr}_2(\text{WO}_4)_3$  (pale orange),  $\text{Nd}_2(\text{WO}_4)_3$  (yellow),  $\text{Sm}_2(\text{WO}_4)_3$  (olive),  $\text{Eu}_2(\text{WO}_4)_3$  (green),  $\text{Gd}_2(\text{WO}_4)_3$  (pale blue),  $\text{Tb}_2(\text{WO}_4)_3$  (blue),  $\text{Dy}_2(\text{WO}_4)_3$  (violet), and  $\text{Ho}_2(\text{WO}_4)_3$  (magenta).

directions, with Miller indices: (110), (−110), (112), (022), (200), (202), (112), and (−113). These results are very similar for both PBE [ $\text{La}_2(\text{WO}_4)_3$ ,  $\text{Nd}_2(\text{WO}_4)_3$ , and  $\text{Gd}_2(\text{WO}_4)_3$ ], and PBEsol [ $\text{La}_2(\text{WO}_4)_3$ ,  $\text{Dy}_2(\text{WO}_4)_3$ ] approximations. In order to compare the different compounds among themselves and look for more quantitative correlations, we will continue to delve into these anomalies studying the effect on the compression of the experimental lattice parameters for the complete family.

In Fig. 5 we represent the evolution of the experimental lattice parameters as a function of the pressure for the La–Ho tungstates. The observed monotonous compression of the experimental lattice parameters indicates that the compounds with larger ionic radius do not undergo any phase transition until 6.0, 7.2, 7.3, and 8.5 GPa, for the La, Ce, Pr, and Nd tungstates, respectively. These pressures correspond to the minimum of the  $a$  parameter. After that, satellite peaks appear in the patterns shown in Figs. 3 and S3. At these pressures, the four compounds undergo a phase transition where the average unit cell volume is compressed around 5%, 4%, 3%, and 2.5% for La, Ce, Pr, and Nd, respectively.

After this first transition, the experimental lattice parameters  $a$  and  $c$  feature a more anisotropic evolution; the parameter  $c$  decreases rapidly while the parameter  $a$  increases

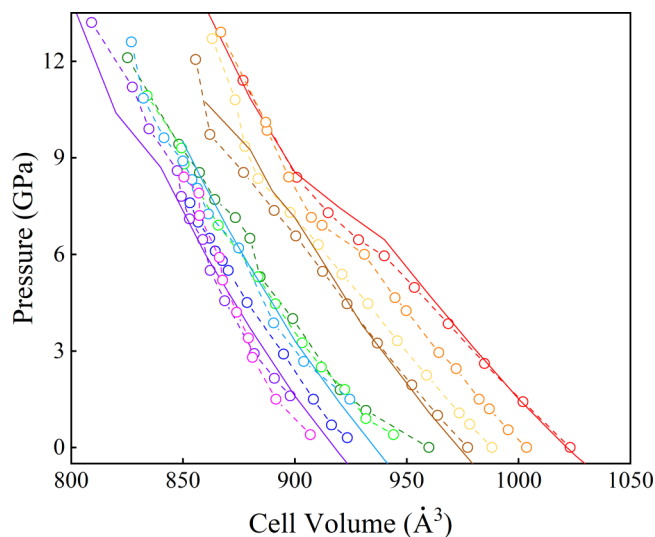


FIG. 6.  $P(V)$  curve for  $\text{La}_2(\text{WO}_4)_3$  (red),  $\text{Ce}_2(\text{WO}_4)_3$  (orange),  $\text{Pr}_2(\text{WO}_4)_3$  (pale orange),  $\text{Nd}_2(\text{WO}_4)_3$  (yellow),  $\text{Sm}_2(\text{WO}_4)_3$  (olive),  $\text{Eu}_2(\text{WO}_4)_3$  (green),  $\text{Gd}_2(\text{WO}_4)_3$  (pale blue),  $\text{Tb}_2(\text{WO}_4)_3$  (blue),  $\text{Dy}_2(\text{WO}_4)_3$  (violet), and  $\text{Ho}_2(\text{WO}_4)_3$  (magenta).

showing a NLC, and the  $\beta$  angle experiences a jump toward low angles. Compressibility coefficients for both lattice parameters were estimated into the NLC region reaching the maximum values for  $\text{La}_2(\text{WO}_4)_3$ :  $\beta_a = -3.5 \text{ TPa}^{-1}$  and  $\beta_c = 15 \text{ TPa}^{-1}$ . The correlation with the ionic radii is clear.

The compressibility of the experimental  $a$  and  $c$  cell parameters and the  $\beta$  angle for the Sm-Ho tungstates is a little bit

TABLE II.  $V_0$ , and  $B_0$  parameters of second-order Birch-Murnaghan equation of state in the range 0–5.0 GPa (up) and 0–7.5 GPa (down).

	$V_0$	$V_0$	$B_0$	$B_0$
	Expt.	Theor.	Expt.	Theor.
$\text{La}_2(\text{WO}_4)_3^a$	1023.2(8) <sup>a</sup>	1026(4) <sup>a</sup>	63.4(8) <sup>a</sup>	59.2(1) <sup>a</sup>
	1024.9(8)	1024.916(4)	60(1)	59.715(5)
	1024.9(8)	1024.917(3)	60(1)	59.715(4)
$\text{Ce}_2(\text{WO}_4)_3$	1003.8(5)		69(1)	
	1003.8(4)		68.7(6)	
$\text{Pr}_2(\text{WO}_4)_3$	989.2(6)		66(1)	
	991(1)		62(1)	
$\text{Nd}_2(\text{WO}_4)_3$	977.8(4)	978.9204(9)	68.8(7)	65.923(1)
	979(1)	978.9197(8)	66(1)	65.925(1)
$\text{Sm}_2(\text{WO}_4)_3$	954(5)		58(6)	
	951(4)		67(6)	
$\text{Eu}_2(\text{WO}_4)_3$	945(3)		69(6)	
	944(2)		74(4)	
$\text{Gd}_2(\text{WO}_4)_3$	941(1)	940.6188(8)	69(3)	70.925(1)
	941(1)	940.6179(7)	71(1)	70.928(1)
$\text{Tb}_2(\text{WO}_4)_3$	927(1)		74(3)	
	927.1(7)		76(1)	
$\text{Dy}_2(\text{WO}_4)_3$	920(1)	918.9301(8)	84(4)	93.010(3)
	919(2)	918.9303(7)	93(5)	93.009(1)
$\text{Ho}_2(\text{WO}_4)_3$	911(2)		86(8)	
	908(2)		104(8)	

<sup>a</sup>Values from Ref. [23].

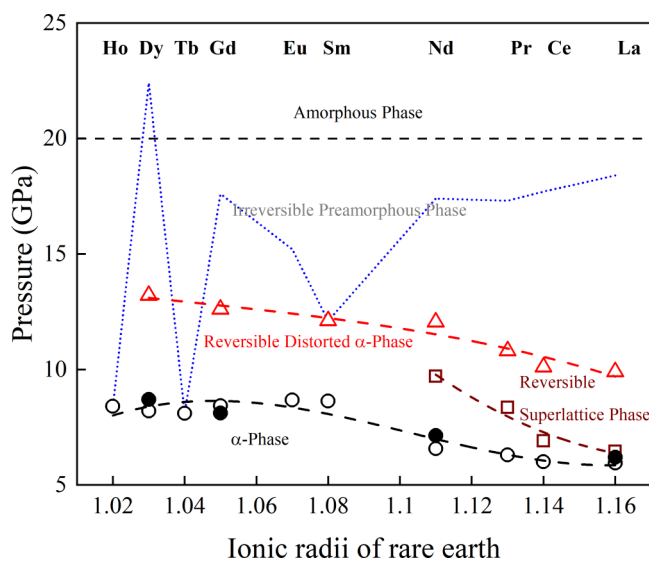


FIG. 7. Phase diagram representing the phase transitions and other anomalies obtained by compressing the  $\alpha\text{-RE}_2(\text{WO}_4)_3$  family. Open (experimental) and filled (theoretical) black circles indicate the pressures in which the  $a$  parameter is minimum. Pressures of the expected transition to the reversible *superlattice* phase are shown by brown squares. The pressures of the expected transition to the *preamorphous* phase are shown by dark red triangles. Also, the range of the measured pressures are marked with a dashed blue line.

different from that observed for the La-Nd tungstates, with a smoother behavior at moderate pressures and no indication of the first phase transition observed in the La-Nd series, in line with the previous discussion about the diffraction patterns. For these heavier tungstates, the minimum of the  $a$  parameter takes place at the pressures where an anisotropic behavior was beginning to be detected (at 7.14, 7.1, 7.25, 7.6, 7.8, and 7.9 GPa). Compressibility coefficients for both parameters were estimated into the NLC region (see the Supplemental Material) reaching the maximum values for  $\text{Dy}_2(\text{WO}_4)_3$ :  $\beta_a = -6.5 \text{ TPa}^{-1}$  and  $\beta_c = 10 \text{ TPa}^{-1}$ ; the correlation of the coefficients with the ionic radii is not so clear.

In Fig. 6 the measured pressures are plotted vs the corresponding unit cell volumes. A second order Birch-Murnaghan equation of state for the low pressure phase of the La-Ho tungstates was used for the fittings, whose results are shown in Table II. We observe a good agreement between the experimental and theoretical results, in addition to an expected stiffness of the rare earth tungstates when the ionic radii decrease is observed. However, there is a clear softening for the lighter compounds corresponding to the pressure interval in which the lattice parameter  $a$  experiences the NLC. The  $\text{Dy}_2(\text{WO}_4)_3$  compound, with larger negative coefficient among the heavier compounds, also shows a theoretical softening at higher pressures, which is not clearly seen in the experimental results.

Finally, in Fig. 7 we summarize the possible pressure range for the different phases in the family  $\alpha\text{-RE}_2(\text{WO}_4)_3$ . In addition, the range of measured pressures is indicated with a dashed blue line. Both the  $\alpha$  phase and the distorted  $\alpha$  phase are differentiated by the dashed black line that fits the pressures (marked with black circles), corresponding to

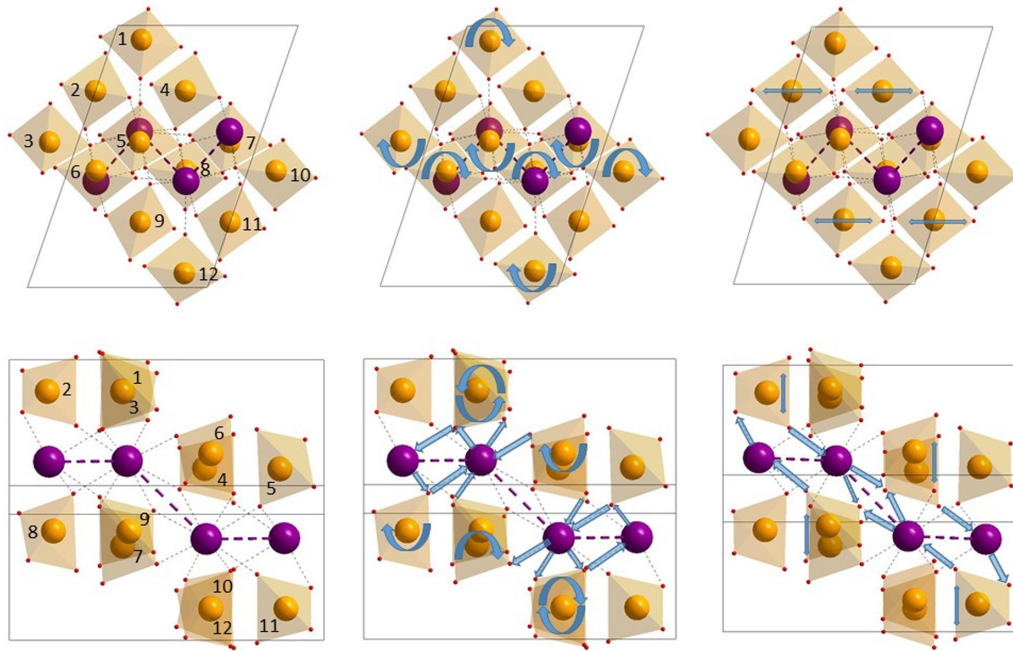


FIG. 8. The theoretical structure of  $\text{Dy}_2(\text{WO}_4)_3$  from the DFT simulations, viewed along the  $b$  axis (top) and through the plane  $(-1, 0, 2)$  (bottom) at the three selected pressures of 4.5 GPa (left), 8.9 GPa (center), and 16.8 GPa (right). The Dy atoms are purple and the W atoms are orange. The shortest Dy ...Dy contacts are indicated as dashed purple lines. Polyhedral Dy ...O contacts are drawn in order to follow the more important movements: (1) Rotation of less symmetric tetrahedra until reaching the minimum of the  $a$  parameter and the  $RE \dots RE \dots RE$  angle. (2) Elongation of the more symmetric tetrahedra improving their alignment along the  $a$  axis and leading to the opening of the  $RE \dots RE \dots RE$  angle.

the minimum of the parameter  $a$ ; the open circles indicate the experimental pressure and the black-filled circles indicate the theoretical ones. This distorted  $\alpha$  phase is not a new real phase, but the line shows that the compression starts to be more anisotropic at lower pressures for rare earth compounds with larger ionic radii. The brown squares indicate the pressures at which the satellite peaks appeared and were refined considering that the parameter  $a$  is tripled; squares are fitted with a brown dashed line. Above this line, the lighter compounds (located on the right in Fig. 7) undergo a transition to the new phase called “reversible superlattice.” When the rare earth ionic radii of these molybdates increase, the phase transitions take place at higher pressures. The dark red triangles indicate the pressures of the transition to the *preamorphous* phase, which occurs in all compounds; these triangles are fitted by a dashed line. This phase appears at higher pressures for compounds with shorter ionic radii of their rare earths. The smaller shift of the broader Bragg peaks led us to the conclusion that, around these pressures, all compounds undergo an irreversible transition from either the distorted  $\alpha$  phase or the *superlattice* to the *preamorphized* state. In the case of  $\text{Dy}_2(\text{WO}_4)_3$ , the transition to the *superlattice* phase and the *preamorphous* phase coincide in the same pressure. The amorphous phase is expected to occur around 20 GPa, although it could develop at lower pressures for lighter tungstates, as is the case with rare earth molybdates [19,21].

#### D. Structural mechanisms

We can go further in the description of the pressure effect on the  $\alpha$  phase and relate the unusual pressure dependence

of the  $a$  parameter to the rotation deformation of the  $\text{WO}_4^{2-}$  groups and the displacement of the  $RE^{3+}$  cations. For this analysis we will use the results of our theoretical calculations. With a view to understand the structural origin of the observed anomalies, and in particular the negative expansion of the  $a$  parameter, we have examined in detail the theoretical crystal structure of the studied compounds at three pressures: below the maximum compression (minimum value) of the  $a$  parameter, at the minimum, and above that minimum. In Fig. 8 we show two views of the simulated crystal structure of  $\alpha\text{-Dy}_2(\text{WO}_4)_3$  depicting the main movements of the  $RE$  atoms and the tetrahedral groups [a similar description stands for  $\text{Gd}_2(\text{WO}_4)_3$  and  $\text{Nd}_2(\text{WO}_4)_3$ ]. As pressure increases, the less symmetric tetrahedra rotate along the  $b$  axis until the pressure corresponding to the minimum of the  $a$  parameter is reached. Above that pressure, the more symmetric tetrahedra become slightly elongated along the  $a$  axis. These tetrahedra tend to get a better alignment along the  $a$  axis, forming a more compact crystal packing at higher pressures.

Comparing the structures at 0 GPa and at other different pressures we find that the bond lengths and angles in the  $\text{WO}_4^{2-}$  units are almost constant (with variations of less than 2%) within the interval studied. The  $\text{WO}_4^{2-}$  groups appear to shift “rigid,” whereas the evolution of all the oxygen-bridge lengths and angles  $RE(W) \dots O \dots W(RE)$ , which are more flexible, would help to explain the rotation of the tetrahedrons and the displacement of the rare earth atoms (less bonded than the W atoms). In the  $\alpha$  phase, the oxygen atoms of both tetrahedra belong to the oxygen bridges between the two closer rare earths forming  $RE \dots RE \dots RE$  zigzag chains along

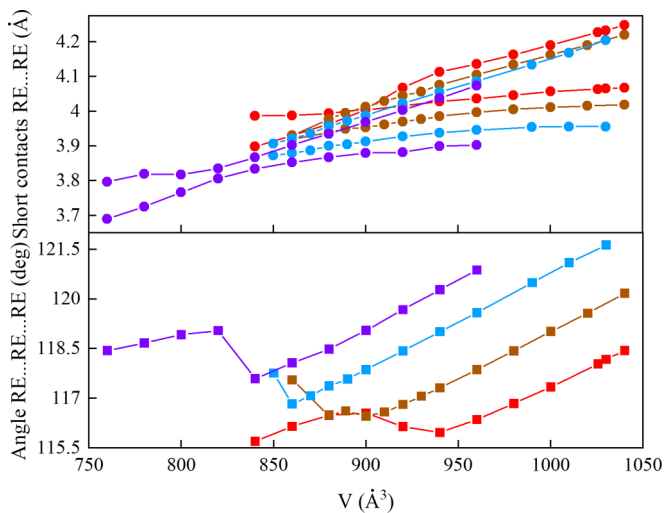


FIG. 9. Calculated pressure dependence of the  $RE..RE$  contact length and the  $RE...RE...RE$  angle for  $La_2(WO_4)_3$  (red)  $Nd_2(WO_4)_3$  (yellow),  $Gd_2(WO_4)_3$  (blue), and  $Dy_2(WO_4)_3$  (violet).

the  $a$  and  $b$  axes (Fig. 8). The changes in these bridges play a major role in the alignment of the tetrahedrons along the  $a$  axis, which is compatible with the aforementioned rotation and alignment of the rigid  $WO_4^{2-}$  groups. This description can also be understood as changes in the chains which drive the rotation and elongation of the tetrahedral groups. The evolution of these singular  $RE...RE...RE$  contacts can be considered to be primarily responsible for the abnormalities observed in the lattice parameter  $a$ . In Fig. 9 we show the results of the theoretical pressure dependence of the  $RE...RE$  lengths and  $RE...RE...RE$  angles. The pressure dependence of the angles is identical to that of the lattice parameter  $a$  in these pressure ranges. The two types of  $RE...RE$  distances decrease reaching a similar value at the pressure at which the  $a$  parameter reaches its minimum value.

We can compare the pressure and thermal dependence of the crystal structures in molybdates with the theoretical evolution under pressure in tungstates. For the La-Ho tungstates the experimental pressure at the minimum of the  $a$  parameter and the experimental and theoretical bulk moduli are slightly below those for the molybdates, so that the tungstates are slightly softer than the molybdates (they are also less dense). For instance, the anomalous pressure dependence of the  $a$  parameter has been explained in a similar way for  $\alpha$ - $Eu_2(MoO_4)_3$  [22]. A similar explanation has also been presented in the case of the thermal dependence of the  $a$  parameter in  $\alpha$ - $Eu_2(MoO_4)_3$  and  $\alpha$ - $Sm_2(MoO_4)_3$  [27,28].

The response to compression of other compounds with related scheelite structures can be compared with that of the rare earth tungstates and molybdates of our study. For example, the evolution of the fergusonite structures (ferroelastic) of denser  $BaWO_4$ ,  $SrWO_4$ , and  $CaWO_4$  show a similar characteristic to those observed in the tungstates of our study. The rotation (tilts) of the  $WO_4$  groups implies the anisotropic behavior of the two lattice parameters which have the same length at the paraelastic scheelite phase and this results in a NLC coefficient for one of them [16,53] at higher pressure. Moreover, the sequence of high pressure structures for most rare earth vanadates has been experimentally determined upon the intensive

investigation carried out during the last decade [54–57]. At ambient conditions, the rare earth vanadates crystallize in the tetragonal zircon type structure, with the exception of  $LaVO_4$  [55,56]. Under moderate compression, these compounds undergo transformations to denser phases: the monazite type structure for the larger rare earth ions, and the scheelite type structure for the smaller ones. The transition pressures and the percentage of the volume collapses at the transition are similar to those found in rare earth tungstates. A more similar evolution under pressure and temperature can be followed in detail in the crystal structures observed for  $LaNbO_4$  at different pressures [58] and temperatures [59]. An anomalous expansion and compression of the  $a$  parameter has been measured upon increase of either pressure or temperature from ambient conditions and has been related to the stiffness of the  $NbO_4$  groups. There are fewer structural studies under high pressure for ferroelastic niobates compared with other families [60,61], and in particular amorphization has not been so far reported for any of its members. The systematic study of families of ferroelastic compounds with the same crystalline structure at room conditions is crucial to fully understand their response to temperature and pressure.

Comparing to other structural types (in a way related to the oxygen bridges and  $RE...RE...RE$  chains), the competition between the distances K-F and V-O and the angles K-F-K and V-O-V and the “collapsible umbrella” structure gives rise to the nonmonotonic pressure dependence of the  $a$  parameter in the layered structures of  $KB_2BO_3F_2$  [62],  $(NH_4)_2V_3O_8$  [63], and  $BiB_3O_6$  [64,65], causing the unique negative compression observed in these inorganic materials (with bulk modulus of 31, 35, and 38 GPa, respectively). The first of these compounds displays experimentally a negative area compression in the range 3–10 GPa ( $\beta_a = -50 \text{ TPa}^{-1}$ ), reaching amorphization at 45 GPa.  $(NH_4)_2V_3O_8$ , undergoes a phase transition in the range 2.5–3.5 GPa with a volume collapse of 3% after which the lattice parameter  $a$  expands ( $\beta_a = -50 \text{ TPa}^{-1}$ ) [58]. Alongside the roles of the V-O lengths and the V-O-V angles, the phase transition is also reflected in the change of environment around the interlayer  $NH_4^+$  cation, similarly to the observed distortions predicted for  $RE$  polyhedra and vacancies in molybdates and tungstates.  $BiB_3O_6$  exhibits a unique large and persistent (from 0 to 6.5 GPa) NLC response ( $\beta_a = -6.4 \text{ TPa}^{-1}$ ) [65]. Above the critical pressure of 6.5 GPa, a structural phase transition occurs where all lattice parameters have positive compressibility. Its crystal structure can be described as a layer structure consisting of alternating layers of borate anions and bismuth cations, where the lone pair on the  $Bi^{3+}$  acts as “umbrella stands” [65]. The mechanisms responsible for axial anisotropic or negative compression in trimolybdates and tritungstates are between those of harder ferroelastics (tungstates, vanadates, and niobates), given by polyhedral tilts, and those of softer compounds with larger negative expansion arisen from framework hinging, including helical or zigzag chains, wine rack, etc.

Finally, we suggest that the amorphous phase may be viewed as a defective long-period modulated scheelite phase, in a way similar to how some perovskite and zeolite minerals have been described under high pressure [66,67]. More recently, Guo *et al.* [68] have found how stacking faults multiply the  $c$  axis length in the fluorine-beryllium borates family, in

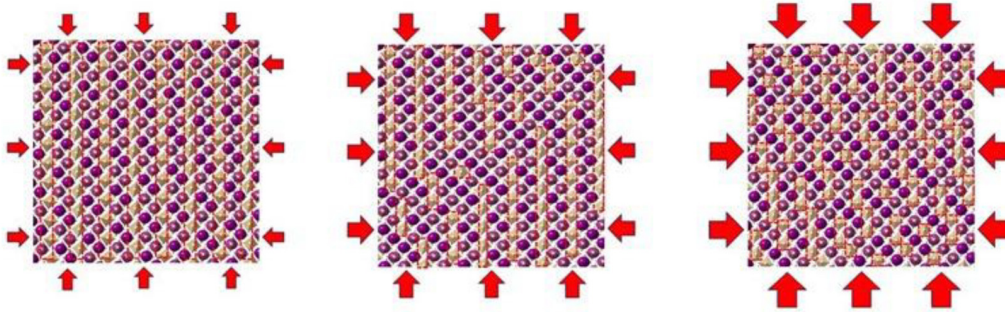


FIG. 10. Different orderings of the rare earth atoms (in purple) and vacancies (shown within orange rectangles that show the  $\text{WO}_4^{2-}$  tetrahedra), which are observed in  $\alpha\text{-RE}_2(\text{MoO}_4)_3$  (left); and simulated with the metric:  $(0.63)\mathbf{a}^* + (0.68)\mathbf{b}^*$  (middle) and with the metric:  $(0.5)\mathbf{a}^* + (0.8)\mathbf{b}^*$  (right).

a way similar to what will be explained here. In  $\text{RE}_2(\text{WO}_4)_3$  compounds, the opening of the  $\text{RE}\dots\text{RE}\dots\text{RE}$  angle destabilizes the structure and can drive the displacement of the  $\text{RE}^{3+}$  cations towards the vacancies, which become also more distorted. This process is irreversible as the vacancies, which were originally aligned along channels parallel to the  $a$  axis (the blocks indicated in Fig. 10), can collapse undergoing a significant structural rearrangement. This can be described in similar terms as those used by Logvinovich *et al.* [51] in order to explain the satellite peaks that appear at room conditions in  $\text{Pr}_2(\text{MoO}_4)_3$ : the regular channels can be interrupted by a few defects, comprising blocks of vacancy clusters. The threshold of amorphization shows an increase in the number of such defects. XRD experiments at high pressure show that all  $\text{RE}_2(\text{WO}_4)_3$  [and  $\text{RE}_2(\text{MoO}_4)_3$ ,  $\text{RE} = \text{La-Ho}$ ] can become amorphous above 20 GPa (which is a pressure lower than observed for other related scheelite compounds). It is difficult to provide precise values for the amorphization pressure for the different compounds and their correlation with the size of the rare earth, because they were measured using different experimental setups and pressure intervals. One can argue that the presence of these blocks of rare earth vacancies associated to subsequent atomic displacements build the *preamorphous* phase in an irreversible process without memory of the initial structure. Note that the appearance and increase of satellite peaks at higher pressures can be related to the loss of periodicity caused by stacking defects. In Fig. 10 we simulate the stages of this process for different distributions of RE atoms. In the first stages of compression, the  $\alpha$  phase is maintained (first panel). At the second and third panels, the defects form new blocks (clusters of vacancies) decreasing in size. The distribution of vacancies was generated from the tetragonal scheelite structure (with  $a = b$ ) adding, respectively, the modulation vectors  $(2/3)\mathbf{a}^* + (2/3)\mathbf{b}^*$ . The second and third panels correspond to the metric  $(0.63)\mathbf{a}^* + (0.68)\mathbf{b}^*$  and  $(0.5)\mathbf{a}^* + (0.8)\mathbf{b}^*$ , respectively. The occupation factor for the rare earth was modeled by a Crenel function [69].

#### IV. CONCLUSIONS

The comparative analyses of the experimental and theoretical pressure dependencies of the lattice parameters and the predicted crystalline structure revealed the following results.

At low and moderate pressure (from 0 to 6–7.5 GPa) the behavior of  $\text{RE}_2(\text{WO}_4)_3$  compounds does not show any striking change with isotropic pressure dependence; our experimental and theoretical results are in good agreement at this stage. Past the minimum experimental value of the parameter  $a$ , reached between 6 and 7.9 GPa for La-Ho tungstates (increasing when the ion radius decreases) the behavior is more anisotropic, including a negative linear compression of the parameter  $a$ . From the calculated atomic coordinates, we described, in some detail, the effect of the pressure on the  $\alpha$  phase, and the anomalous pressure dependence of the  $a$  parameter through the opening of the angles  $\text{RE}\dots\text{RE}\dots\text{RE}$  and the shortening of the  $\text{RE}\dots\text{RE}$  contacts. The unusual NLC occurs after rotation and alignment of the rather rigid  $\text{WO}_4$  tetrahedra along the  $a$  axis, and it is correlated with the elongation of the tetrahedra, driving the movement of the rare earth atoms in these chains. The results of a comparative study with other compounds (with similar structural motifs and displaying NLC) place this family between the ferroelastic fergusonites (with rigid  $\text{WO}_4$  units connected to more flexible  $\text{REO}_8$  polyhedra) and compounds with hinge frameworks (in our case  $\text{RE}\dots\text{RE}\dots\text{RE}$  chains) where the NLC is outstanding.

In addition, the experimental results show up to two possible phase transitions. The experimental anomalous behavior of the lattice parameters is most noticeable in the case of La-Nd tungstates. A first reversible phase transition between 6 and 8.5 GPa was observed which is distinguished by a jump in the cell parameters and the appearance of the modulated (tripled) phase and a more anisotropic behavior (called a *superlattice* phase). These two phases are considerably more compressible, suggesting a more deformable  $\text{REO}_8$  polyhedron (and surroundings of the vacancies) with lower transition pressures as the rare earth's ionic radius increases. The second phase transition is irreversible for all compounds at 10.5–13.5 GPa and without apparent major changes in volume. The lattice parameters are independent of pressure in this new *preamorphous* phase. We have explained this behavior because successive stacking faults appear between the  $\text{RE}\dots\text{RE}\dots\text{RE}$  chains and the blocks of vacancies forming clusters (chains and vacancies). In general, this transition occurs at lower pressures for lanthanides with larger ionic radii, because the collapse of the block of vacancies is easier to achieve. From decompression experiments, we verified the irreversibility of this transition. Although PIA was only

fully achieved for  $\text{Dy}_2(\text{WO}_4)_3$  (the only compound measured at pressures above 20 GPa), our survey shows that  $\text{RE}_2(\text{WO}_4)_3$  compounds reach PIA around this pressure. In turn, the described mechanisms would explain that these compounds amorphize at lower pressure than other compounds with scheelite or related structures.

These high pressure studies have been systematically carried out on the entire  $\text{RE}_2(\text{WO}_4)_3$  family of compounds with  $\text{RE} = \text{La-Ho}$ , which crystallize in the  $\alpha$  phase (modulated scheelite). The possibility of working with the whole family, performing their synthesis, comparing their diffraction data under ambient conditions and under pressure (with different instruments), and performing theoretical DFT simulations for some of them, has allowed us to reach a better understanding, with conclusive results, which would have been more difficult to achieve for isolated samples in individual experiments. As far as we know, the  $\alpha$  phase is exclusive to rare earth tungstates and molybdates. The interest of this study lies in the particular ordering of its stoichiometric vacancies, constructing a modulated scheelite structure that is monoclinic, where vacancies are forming alternating channels along the  $a$  axis with zigzag chains for the shortest  $\text{RE} \dots \text{RE}$  contacts.

Finally, the role and importance of the defects in the material properties is highlighted. Possible stacking faults in our materials are compatible with an incommensurate modulation associated to changes in the occupations of atomic sites and vacancies. We have simulated different degrees of defects to explain the *preamorphous* phase by calculating different modulations of the scheelite crystal structure with different propagation vectors. The phenomenon of pressure-induced amorphization is difficult to explain. In compounds with coordination polyhedra bonded by the corners, which have open structures, PIA is generally described by the deformation of the polyhedra and changes in their coordination numbers. This is not exactly our case, where  $\text{RE} \dots \text{RE} \dots \text{RE}$  chains and vacancy blocks also play an important role. This family of compounds could play an important role in the search

for new materials or metamaterials with the most extreme NLC or zero compression and for the densification of new defective materials. The control of their structural characteristics (structural motifs and defects) could allow us to obtain analog solids with better electronic, optical, mechanical, and thermodynamic properties.

#### ACKNOWLEDGMENTS

C.G.-S., C.G.-A., V.L., J.L.-S., A.M., and M.E.T. wish to thank Prof. A. Muñoz for his support as head leader of the high pressure research projects in which we have been involved for many years. All of us would like to acknowledge the advice and support of the local contacts Dr. A. Kleppe from DIAMOND, Dr. I. Peral, and Dr. F. Fauth from ALBA. All of us acknowledge Diamond Light Source [70] funders, the STFC and the Wellcome Trust and ALBA [71] funders, the Catalan and Spanish governments, and to all Spanish government ministries that have funded research projects over the past ten years. A.M. and V.L. acknowledge the financial support from MCIN/AEI (Spain) through Projects PID2019-106383GB-C43/C44. A.M. acknowledges the MALTA Consolider Ingenio 2010 Network, MAT2015-71070-REDC and RED2018-102612-T (MINECO, Spain).

L.M. and X.V. performed the synthesis and participated in the ALBA experiments with V.L. and M.E.T.; D.S. measured in Xcalibur with the help of N.P.S.; M.C.G.-A. and J.L.-S. participated in the DIAMOND experiment. N.P.S. devised the work and started the analysis of the data as part of her Ph.D. thesis, supervised by C.G.-S. and M.E.T. Her long illness and death in 2018 prevented her from finishing the work. C.G.-S., G.G.deC., and I.T.M.-M. continued the analysis of the data, finishing the experimental work. J.L.-S. and A.M. performed the theoretical calculations. C.G.-S. and A.M. coordinated the discussion and writing in which J.L.-S., M.E.T., and G.G.deC. have also participated. All the authors reviewed the work and contributed with important corrections and suggestions.

- 
- [1] M. Maczka, A. G. Souza Filho, W. Paraguassu, P. T. C. Freire, J. Mendes Filho, and J. Hanuza, Pressure-induced structural phase transitions and amorphization in selected molybdates and tungstates, *Prog. Mater. Sci.* **57**, 1335 (2012).
  - [2] P. Richet and P. Gillet, Pressure-induced amorphization of minerals: A review, *Eur. J. Mineral.* **9**, 907 (1997).
  - [3] A. M. Kaczmarek and R. Van Deun, Rare earth tungstate and molybdate compounds from 0D to 3D architectures, *Chem. Soc. Rev.* **42**, 8835 (2013).
  - [4] V. A. Isupov, Ferroelectric and ferroelastic phase transitions in molybdates and tungstates of monovalent and bivalent elements, *Ferroelectrics* **322**, 83 (2005).
  - [5] T. Varga, A. P. Wilkinson, C. Lind, W. A. Bassett, and C. S. Zha, High pressure synchrotron X-ray powder diffraction study of  $\text{Sc}_2\text{Mo}_3\text{O}_{12}$  and  $\text{Al}_2\text{W}_3\text{O}_{12}$ , *J. Phys.: Condens. Matter* **17**, 4271 (2005).
  - [6] J. S. O. Evans, T. A. Mary, and A. W. Sleight, Negative thermal expansion in a large molybdate and tungstate family, *J. Solid State Chem.* **133**, 580 (1997).
  - [7] A. Zaoui and W. Sekkal, Pressure-induced softening of shear modes in Wurtzite ZnO: A theoretical study, *Phys. Rev. B* **66**, 174106 (2002).
  - [8] A. B. Cairns and A. L. Goodwin, Negative linear compressibility, *Phys. Chem. Chem. Phys.* **17**, 20449 (2015).
  - [9] A. B. Cairns, J. Catafesta, C. Levelut, J. Rouquette, A. Van Der Lee, L. Peters, A. L. Thomson, V. Dmitriev, J. Haines, and A. L. Goodwin, Giant negative linear compressibility in zinc dicyanoaurate, *Nat. Mater.* **12**, 212 (2013).
  - [10] S. C. Abrahams and J. L. Bernstein, Crystal structure of the transition metal molybdates and tungstates. II. Diamagnetic  $\text{Sc}_2(\text{WO}_4)_3$ , *J. Chem. Phys.* **45**, 2745 (1966).
  - [11] D. H. Templeton and A. Zalkin, Crystal structure of europium tungstate, *Acta Crystallogr.* **16**, 762 (1963).
  - [12] W. Jeitschko, Crystal structure of  $\text{La}_2(\text{MoO}_4)_3$ , a new ordered defect scheelite type, *Acta Crystallogr., Sect. B* **29**, 2074 (1973).

- [13] W. Jeitschko, A comprehensive X-ray study of the ferroelectric–ferroelastic and paraelectric–paraelastic phases of  $\text{Gd}_2(\text{MoO}_4)_3$ , *Acta Crystallogr., Sect. B* **28**, 60 (1972).
- [14] A. Arakcheeva, D. Logvinovich, G. Chapuis, V. Morozov, S. V. Eliseeva, J. C. G. Bünzli, and P. Pattison, The luminescence of  $\text{Na}_x\text{Eu}_{3+(2-x)/3}\text{MoO}_4$  scheelites depends on the number of Eu-clusters occurring in their incommensurately modulated structure, *Chem. Sci.* **3**, 384 (2012).
- [15] R. Lacomba-Perales, J. Ruiz-Fuertes, D. Errandonea, D. Martínez-García, and A. Segura, Optical absorption of divalent metal tungstates: Correlation between the band-gap energy and the cation ionic radius, *Europhys. Lett.* **83**, 37002 (2008).
- [16] D. Errandonea and F. J. Manjón, Pressure effects on the structural and electronic properties of  $\text{ABX}_4$  scintillating crystals, *Prog. Mater. Sci.* **53**, 711 (2008).
- [17] A. Arakcheeva and G. Chapuis, Capabilities and limitations of a (3+d)-dimensional incommensurately modulated structure as a model for the derivation of an extended family of compounds: Example of the scheelite-like structures, *Acta Crystallogr., Sect. B* **64**, 12 (2008).
- [18] E. T. Keve, S. C. Abrahams, and J. L. Bernstein, Ferroelectric ferroelastic paramagnetic  $\beta$ - $\text{Gd}_2(\text{MoO}_4)_3$  crystal structure of the transition-metal molybdates and tungstates. VI, *J. Chem. Phys.* **54**, 3185 (1971).
- [19] A. Jayaraman, S. K. Sharma, Z. Wang, and S. Y. Wang, Pressure-induced amorphization in the  $\alpha$ -phase of  $\text{Nd}_2(\text{MoO}_4)_3$  and  $\text{Tb}_2(\text{MoO}_4)_3$ , *Solid State Commun.* **101**, 237 (1997).
- [20] C. Guzmán-Afonso, J. López-Solano, C. González-Silgo, S. F. León-Luis, E. Matesanz, and A. Mujica, Pressure evolution of two polymorphs of  $\text{Tb}_2(\text{MoO}_4)_3$ , *High Press. Res.* **34**, 184 (2014).
- [21] O. Le Bacq, D. Machon, D. Testemale, and A. Pasturel, Pressure-induced amorphization mechanism in  $\text{Eu}_2(\text{MoO}_4)_3$ , *Phys. Rev. B* **83**, 214101 (2011).
- [22] C. Guzmán-Afonso, S. F. León-Luis, J. A. Sans, C. González-Silgo, P. Rodríguez-Hernández, S. Radescu, A. Muñoz, J. López-Solano, D. Errandonea, F. J. Manjón, U. R. Rodríguez-Mendoza, and V. Lavín, Experimental and theoretical study of  $\alpha - \text{Eu}_2(\text{MoO}_4)_3$  under compression, *J. Phys.: Condens. Matter* **27**, 465401 (2015).
- [23] N. P. Sabalisck, J. López-Solano, C. Guzmán-Afonso, D. Santamaría-Pérez, C. González-Silgo, A. Mujica, A. Muñoz, P. Rodríguez-Hernández, X. Vendrell, L. Mestres, J. A. Sans, and F. J. Manjón, Effect of pressure on  $\text{La}_2(\text{WO}_4)_3$  with a modulated scheelite-type structure, *Phys. Rev. B* **89**, 174112 (2014).
- [24] C. Hejny and V. S. Minkov, High-pressure crystallography of periodic and aperiodic crystals, *IUCrJ* **2**, 218 (2015).
- [25] J. Marciniak, J. and A. Katrusiak, Direct and inverse relations between temperature and pressure effects in crystals: A case study on o-xylene, *J. Phys. Chem. C* **121**, 22303 (2017).
- [26] H. Fang and M. T. Dove, Pressure-induced softening as common feature of framework structures with negative thermal expansion, *Phys. Rev. B* **87**, 214109 (2013).
- [27] C. Guzmán-Afonso, M. E. Torres, C. González-Silgo, N. Sabalisck, J. González-Platas, E. Matesanz, and A. Mujica, Electrical transport and anomalous structural behavior of  $\alpha$ - $\text{Eu}_2(\text{MoO}_4)_3$  at high temperature, *Solid State Commun.* **151**, 1654 (2011).
- [28] C. Guzmán-Afonso, C. González-Silgo, M. E. Torres, E. Matesanz, and A. Mujica, Structural anomalies related to changes in the conduction mechanisms of  $\alpha$ - $\text{Sm}_2(\text{MoO}_4)_3$ , *J. Phys.: Condens. Matter* **25**, 035902 (2012).
- [29] C. González-Silgo, M. E. Torres, I. T. Martín-Mateos, E. Zanardi, A. Mujica, F. Lahoz, J. López-Solano, and C. Guzmán-Afonso, in *Polarons: Recent Progress and Perspectives* (Nova Science, New York, 2018), Chap. 8.
- [30] G. Kresse and G. Hafner, *ab initio* molecular dynamics for open-shell transition metals, *Phys. Rev. B* **47**, 558 (1993).
- [31] G. Kresse and J. Furthmüller, Efficient iterative schemes for *ab initio* total-energy calculations using a plane-wave basis set, *Phys. Rev. B* **54**, 11169 (1996).
- [32] G. Kresse and D. Joubert, From ultrasoft pseudopotentials to the projector augmented-wave method, *Phys. Rev. B* **59**, 1758 (1999).
- [33] P. E. Blöchl, Projector augmented-wave method, *Phys. Rev. B* **50**, 17953 (1994).
- [34] J. P. Perdew, K. Burke, and M. Ernzerhof, Generalized Gradient Approximation Made Simple, *Phys. Rev. Lett.* **77**, 3865 (1996).
- [35] J. P. Perdew, A. Ruzsinszky, G. I. Csonka, O. A. Vydrov, G. E. Scuseria, L. A. Constantin, X. Zhou, and K. Burke, Restoring the Density-Gradient Expansion for Exchange in Solids and Surfaces, *Phys. Rev. Lett.* **100**, 136406 (2008).
- [36] H. J. Monkhorst and J. D. Pack, Special points for brillouin-zone integrations, *Phys. Rev. B* **13**, 5188 (1976).
- [37] See Supplemental Material at <http://link.aps.org/supplemental/10.1103/PhysRevMaterials.5.123601> for Tables S1a-c, S2a-m, S3a-c, and Figs. S1, S2, S3a-e, S4, and S5.
- [38] A. P. Hammersley, S. O. Svensson, M. Hanfland, A. N. Fitch, and D. Hausermann, Two-dimensional detector software: From real detector to idealised image or two-theta scan, *Int. J. High Press. Res.* **14**, 235 (1996).
- [39] A. Le Bail, Whole powder pattern decomposition methods and applications: A retrospection, *Powder Diffraction.* **20**, 316 (2005).
- [40] J. Rodríguez-Carvajal, Recent advances in magnetic structure determination by neutron powder diffraction, *Physica B (Amsterdam, Neth.)* **192**, 55 (1993).
- [41] I. Halasz, R. E. Dinnebier, and R. Angel, Parametric Rietveld refinement for the evaluation of powder diffraction patterns collected as a function of pressure, *J. Appl. Crystallogr.* **43**, 504 (2010).
- [42] J. G. Moberly, M. T. Bernards, and K. V. Waynant, Key features and updates for origin 2018, *J. Cheminform.* **10**, 5 (2018).
- [43] H. Putz and K. Brandenburg, Diamond-crystal and molecular structure visualization crystal impact, available at <http://www.crystalimpact.com/diamond>.
- [44] J. González-Platas, M. Alvaro, F. Nestola, and R. Angel, EosFit7-GUI: A new graphical user interface for equation of state calculations, analyses and teaching, *J. Appl. Crystallogr.* **49**, 1377 (2016).
- [45] J. Martínez-García, A. Arakcheeva, P. Pattison, V. Morozov, and G. Chapuis, Validating the model of a (3+1)-dimensional incommensurately modulated structure as generator of a family of compounds for the  $\text{Eu}_2(\text{MoO}_4)_3$  scheelite structure, *Philos. Mag. Lett.* **89**, 257 (2009).
- [46] D. Orobengoa, C. Capillas, M. I. Aroyo, and J. M. Pérez-Mato, AMPLIMODES: Symmetry-mode analysis on the Bilbao Crystallographic Server, *J. Appl. Crystallogr.* **42**, 820 (2009).

- [47] J. M. Perez-Mato, D. Orobengoa, and M. I. Aroyo, Mode crystallography of distorted structures, *Acta Crystallogr., Sect. A* **66**, 558 (2010).
- [48] V. A. Morozov, A. Arakcheeva, P. Pattison, K. W. Meert, P. F. Smet, D. Poelman, N. Gauquelin, J. Verbeeck, A. M. Abakumov, and J. Hadermann, KEu (MoO<sub>4</sub>)<sub>2</sub>: Polymorphism, structures, and luminescent properties, *Chem. Mater.* **27**, 5519 (2015).
- [49] S. Klotz, J. C. Chervin, P. Munsch, and G. Le Marchand, Hydrostatic limits of 11 pressure transmitting media, *J. Phys. D: Appl. Phys.* **42**, 075413 (2009).
- [50] D. Errandonea, O. Gomis, P. Rodríguez Hernández, A. Muñoz, J. Ruiz-Fuertes, M. Gupta, S. Achary, A. Hirsch, F. J. Manjón, L. Peters, G. Roth, A. K. Tyagi, and M. Bettinelli, High-pressure structural and vibrational properties of monazite-type BiPO<sub>4</sub>, LaPO<sub>4</sub>, CePO<sub>4</sub>, and PrPO<sub>4</sub>, *J. Phys.: Condens. Matter* **30**, 065401 (2018).
- [51] D. Logvinovich, A. Arakcheeva, P. Pattison, S. Eliseeva, P. Tomes, I. Marozau, and G. Chapuis, Crystal structure and optical and magnetic properties of Pr<sub>2</sub>(MoO<sub>4</sub>)<sub>3</sub>, *Inorg. Chem.* **49**, 1587 (2010).
- [52] N. Garg, C. Murli, A. K. Tyagi, and S. M. Sharma, Phase transitions in Sc<sub>2</sub>(WO<sub>4</sub>)<sub>3</sub> under high pressure, *Phys. Rev. B* **72**, 064106 (2005).
- [53] V. Panchal, N. Garg, H. K. Poswal, D. Errandonea, P. Rodríguez-Hernández, A. Muñoz, and E. Cavalli, High-pressure behavior of CaMoO<sub>4</sub>, *Phys. Rev. Materials* **1**, 043605 (2017).
- [54] D. Errandonea, Exploring the properties of MTO<sub>4</sub> compounds using high-pressure powder x-ray diffraction, *Cryst. Res. Technol.* **50**, 729 (2015).
- [55] O. Ermakova, J. López-Solano, R. Minikayev, S. Carlson, A. Kamińska, M. Glowacki, M. Berkowski, A. Mujica, A. Muñoz, and W. Paszkowicz, A combined study of the equation of state of monazite-type lanthanum orthovanadate using *in situ* high-pressure diffraction and *ab initio* calculations, *Acta Crystallogr., Sect. B* **70**, 533 (2014).
- [56] E. Varghese, S. Kumar, B. Pathak, and S. Sen, Temperature-induced crystallinity and vibrational properties in samarium orthovanadate, *Phys. Rev. B* **101**, 174112 (2020).
- [57] T. Marqueño, D. Errandonea, J. Pellicer-Porres, D. Santamaria-Perez, D. Martínez-García, E. Bandiello, P. Rodríguez-Hernández, A. Muñoz, S. N. Achary, and C. Popescu, Polymorphism of praseodymium orthovanadate under high pressure, *Phys. Rev. B* **103**, 134113 (2021).
- [58] J. W. E. Mariathasan, L. W. Finger, and R. M. Hazen, High-pressure behavior of LaNbO<sub>4</sub>, *Acta Crystallogr., Sect. B* **41**, 179 (1985).
- [59] P. Sarin, R. W. Hughes, D. R. Lowry, Z. D. Apostolov, and W. M. Kriven, High-temperature properties and ferroelastic phase transitions in rare-earth niobates (LnNbO<sub>4</sub>), *J. Am. Ceram. Soc.* **97**, 3307 (2014).
- [60] H. Jiwei, C. Qiao, G. Chan, D. Rucheng, J. Zhang, W. Zhongping, Z. Zengming, and D. Zejun, Raman and luminescence studies on phase transition of EuNbO<sub>4</sub> under high pressure, *J. Rare Earths* **32**, 787 (2014).
- [61] J. Pellicer-Porres, A. B. Garg, D. Vázquez-Socorro, D. Martínez-García, C. Popescu, and D. Errandonea, Stability of the fergusonite phase in GdNbO<sub>4</sub> by high pressure XRD and Raman experiments, *J. Solid State Chem.* **251**, 14 (2017).
- [62] D. H. Yu, M. Avdeev, D. H. Sun, L. Q. Huston, T. B. Shiehl, Q. B. Sun, T. Lu, Q. Gu, H. Liu, J. E. Bradby, N. Yie, Y. Liu, J. Y. Wang, and G. McIntyre, Understanding the unusual response to high pressure in KB<sub>2</sub>BO<sub>3</sub>F<sub>2</sub>, *Sci. Rep.* **7**, 4027 (2017).
- [63] A. Grzechnik, T. Z. Ren, J. M. Posse, and K. Friese, Pressure-induced first-order phase transition in (NH<sub>4</sub>)<sub>2</sub>V<sub>3</sub>O<sub>8</sub> fresnoite: A double coordination change for V<sup>4+</sup> and V<sup>5+</sup>, *Dalton Trans.* **40**, 4572 (2011).
- [64] R. E. Dinnebier, B. Hinrichsen, A. Lennie, and M. Jansen, High-pressure crystal structure of the non-linear optical compound BiB<sub>3</sub>O<sub>6</sub> from two-dimensional powder diffraction data, *Acta Crystallogr., Sect. B* **65**, 1 (2009).
- [65] L. Kang, X. Jiang, S. Luo, P. Gong, W. Li, X. Wu, Y. Li, X. Li, C. Chen, and Z. Lin, Negative linear compressibility in a crystal of α-BiB<sub>3</sub>O<sub>6</sub>, *Sci. Rep.* **5**, 13432 (2015).
- [66] G. C. Serghiou and W. S. Hammack, Pressure-induced amorphization of wollastonite (CaSiO<sub>3</sub>) at room temperature, *J. Chem. Phys.* **98**, 9830 (1993).
- [67] F. G. Alabarse, J. B. Brubach, P. Roy, A. Haidoux, C. Levelut, J. L. Bantignies, O. Cambon, and J. Haines, AlPO<sub>4</sub>-54–AlPO<sub>4</sub>-8 structural phase transition and amorphization under high pressure, *J. Phys. Chem. C* **119**, 7771 (2015).
- [68] S. Guo, X. Jiang, M. Xia, L. Liu, Z. Fang, Q. Huang, R. Wu, X. Wang, Z. Lin, and C. Chen, Structural design of two fluorine-beryllium borates BaMBe<sub>2</sub>(BO<sub>3</sub>)<sub>2</sub>F<sub>2</sub> (M = Mg, Ca) containing flexible two-dimensional [Be<sub>3</sub>B<sub>3</sub>O<sub>6</sub>F<sub>3</sub>]<sub>∞</sub> single layers without structural instability problems, *Inorg. Chem.* **56**, 11451 (2017).
- [69] V. Petricek, M. Dusek, and L. Palatinus, Crystallographic computing system JANA2006: General features, *Z. Kristallogr. Cryst. Mater.* **229**, 345 (2014).
- [70] <https://www.diamond.ac.uk/>.
- [71] <https://www.cells.es/es/>.